Article

Ambient-pressure superconductivity onset above 40 K in $(La,Pr)_3Ni_2O_7$ films

https://doi.org/10.1038/s41586-025-08755-z

Received: 16 November 2024

Accepted: 7 February 2025

Published online: 17 February 2025

Check for updates

Guangdi Zhou[1,4], Wei Lv[1,4], Heng Wang[1,4], Zihao Nie[1,4], Yaqi Chen[1], Yueying Li[1], Haoliang Huang[1,2], Wei-Qiang Chen[1,2], Yu-Jie Sun[1,2], Qi-Kun Xue[1,2,3]✉ & Zhuoyu Chen[1,2]✉

The discovery of Ruddlesden–Popper (RP) bilayer nickelate superconductors under high pressure has opened a new chapter in high-transition-temperature superconductivity[1–8]. However, the high-pressure conditions and presence of impurity phases have hindered comprehensive investigations into their superconducting properties and potential applications. Here we report ambient-pressure superconductivity onset above the McMillan limit (40 K) in RP bilayer nickelate epitaxial thin films. Three-unit-cell-thick $La_{2.85}Pr_{0.15}Ni_2O_7$ pure-phase single-crystal films are grown using the gigantic-oxidative atomic layer-by-layer epitaxy on $SrLaAlO_4$ substrates[9]. Resistivity measurements and magnetic field responses indicate onset transition temperature of 45 K. The transition to zero resistance shows characteristics consistent with a Berezinskii–Kosterlitz–Thouless (BKT) behaviour, with T_{BKT} = 9 K. The Meissner diamagnetic effect is observed at 8 K by using a mutual inductance setup, in agreement with the BKT-like transition. In- and out-of-plane critical magnetic fields show anisotropy. Scanning transmission electron microscopy images and X-ray reciprocal space mappings reveal that the RP bilayer nickelate films adopt a tetragonal phase under roughly 2% coherent epitaxial compressive strain in the NiO_2 planes relative to the bulk. Our findings pave the way for comprehensive investigations of nickelate superconductors under ambient pressure conditions and for exploring superconductivity at higher transition temperatures through strain engineering in heterostructures.

High-transition-temperature (T_C) superconductivity was first discovered in cuprates that consist of stacked superconducting CuO_2 planes[10–13]. In each Cu ion within the Cu–O planes, roughly nine electrons occupy the 3*d* orbitals, with the $3d_{x^2-y^2}$ orbital dominating near the Fermi level. The infinite-layer nickelates with superconducting NiO_2 planes[14], which are structurally analogous to cuprates and share the $3d^9$ configuration, show a comparable electronic structure near the Fermi level, although with weaker oxygen hybridization, placing them closer to the Mott–Hubbard regime[15–24]. By contrast, the recently discovered RP bilayer nickelate superconductors possess a nominal $3d^{7.5}$ configuration, resulting in a distinct electronic structure compared to both cuprates and infinite-layer nickelates[1,7]. Structurally, unlike cuprates and infinite-layer nickelates that lack apical oxygen atoms between the active superconducting planes, the RP bilayer nickelates feature apical oxygens between the adjacent NiO_2 layers, suggesting a possible combined contribution from $3d_{x^2-y^2}$ and $3d_{z^2}$ orbitals[1,6,25–30]. Despite all these differences, bilayer nickelates can host T_C as high as the liquid nitrogen temperature, although only under high-pressure conditions, marking them as a crucial system for understanding the mechanism of high-T_C superconductivity.

Superconductivity in bilayer nickelate $La_3Ni_2O_7$ was first observed at pressures exceeding 14 GPa, with resistance approaching zero[1,2]. Subsequent studies achieved zero-resistance states in both single-crystalline and polycrystalline $La_3Ni_2O_7$ samples under hydrostatic pressure, although the superconducting volume fraction remained low[3,4]. The presence of structural polymorphs, including various RP variants, poses significant challenges and obscures the identification of the phase truly responsible for superconductivity[31–35]. More recent efforts, such as substituting one-third of La with Pr to form $La_2PrNi_2O_7$, have successfully reduced phase intergrowth and improved the bilayer structure purity, which enhance greatly the superconducting volume fraction[5]. Nevertheless, the reliance on high-pressure conditions and the persistence of residual phase inhomogeneities continue to limit comprehensive experimental investigations into underlying superconducting mechanism and potential technological applications of bilayer nickelates. Crucially, whether high T_C above the 40-K McMillan limit is possible under ambient pressure remains an important open question. Here, through substrate-induced compressive strain on epitaxial thin films with rare-earth element substitutions, we have achieved ambient-pressure superconductivity with transition onset at 45 K in pure-phase RP bilayer nickelate thin films, thus opening a direct pathway for experimental studies of its superconducting properties.

$La_{2.85}Pr_{0.15}Ni_2O_7$ thin films are grown on treated (001)-oriented $SrLaAlO_4$ substrates (Fig. 1a) by gigantic-oxidative atomic layer-by-layer

[1]Department of Physics and Guangdong Basic Research Center of Excellence for Quantum Science, Southern University of Science and Technology, Shenzhen, China. [2]Quantum Science Center of Guangdong-Hong Kong-Macao Greater Bay Area, Shenzhen, China. [3]Department of Physics, Tsinghua University, Beijing, China. [4]These authors contributed equally: Guangdi Zhou, Wei Lv, Heng Wang, Zihao Nie. ✉e-mail: xueqk@sustech.edu.cn; chenzhuoyu@sustech.edu.cn

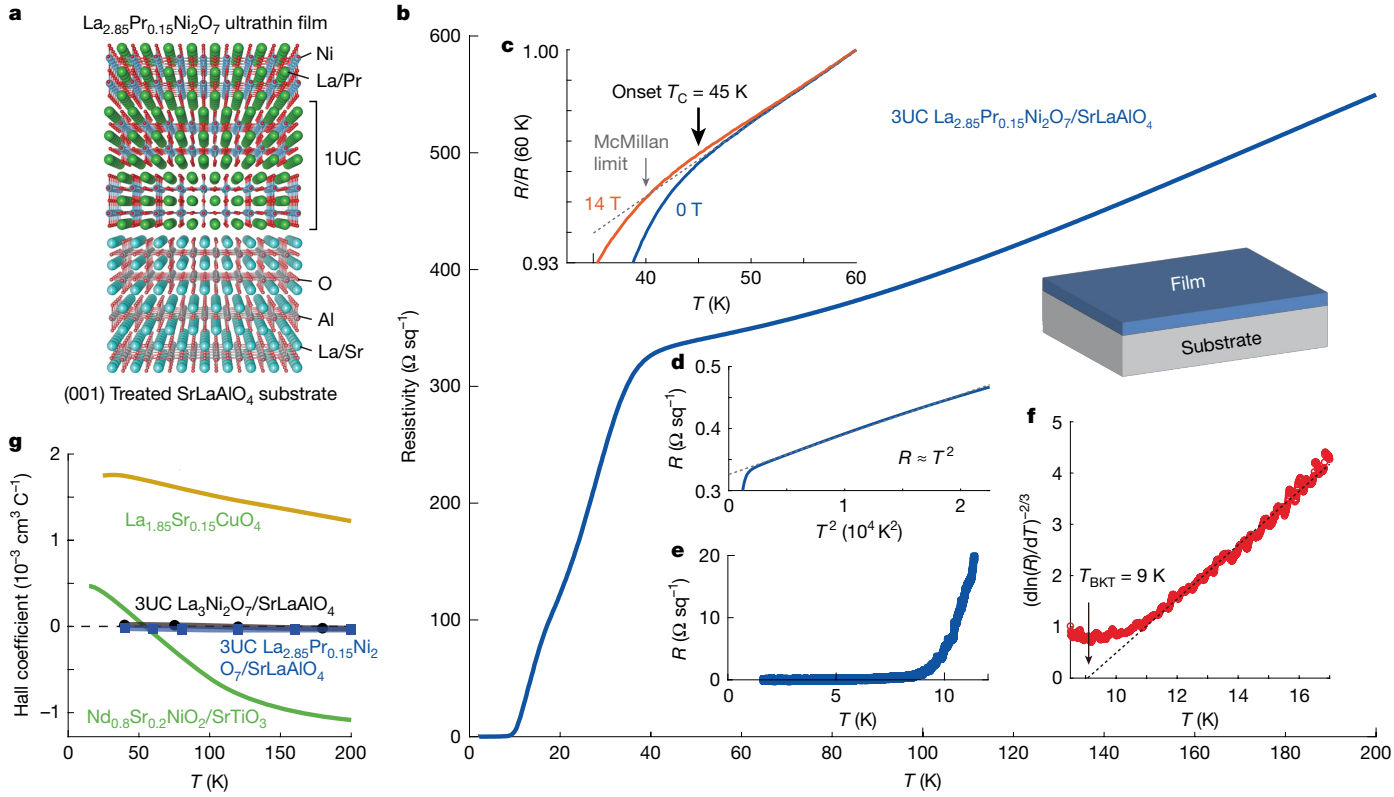

Fig. 1 | Superconducting bilayer nickelate thin film. a, The structural schematic of a $La_{2.85}Pr_{0.15}Ni_2O_7$ bilayer nickelate film grown on treated (001)-oriented $SrLaAlO_4$ substrate. **b**, *R*–*T* curves for a 3UC $La_{2.85}Pr_{0.15}Ni_2O_7$ film on $SrLaAlO_4$. **c**, The onset T_C = 45 K (black down-pointing arrow) is defined as the temperature at which the *R*–*T* curve deviates from the linear fit in the 50–60 K range (grey dashed line) and coincides with the onset of the 14 T magnetic field response (red line). McMillan limit is indicated by a grey down-pointing arrow. The onset T_C above 40 K has been reproduced in 17 samples. Zero-resistance behaviour above 5 K has been observed in 10 samples. **d**, Resistivity as a function of T^2. Grey dashed line is a linear fit. **e**, *R*–*T* curve zoomed in near-zero resistivity. **f**, $(d\ln(R)/dT)^{-2/3}$ versus *T* curve, with linear fit in the 12–17 K range extrapolated to identify T_{BKT} = 9 K (downward pointing arrow). **g**, Temperature-dependent Hall coefficient for bilayer nickelate samples with and without Pr substitutions and references ($La_{1.85}Sr_{0.15}CuO_4$ and $Nd_{0.8}Sr_{0.2}NiO_2/SrTiO_3$) (refs. 14,42).

epitaxy (GOALL-Epitaxy)[9]. In contrast to oxide molecular beam epitaxy or pulsed laser deposition, GOALL-Epitaxy uses different laser ablation targets for different atomic layer under strong ozone oxidation environment (Extended Data Fig. 1a–c). For the growth of a $La_{2.85}Pr_{0.15}Ni_2O_7$ thin film, $La_{0.95}Pr_{0.05}O_x$ and NiO_x targets are alternately ablated according to a set sequence to form periodic stackings of $La_{0.95}Pr_{0.05}O$-NiO_2-$La_{0.95}Pr_{0.05}O$-NiO_2-$La_{0.95}Pr_{0.05}O$. Each period corresponds to half unit cell of the lattice structure. The growth process is monitored in situ with reflective high-energy electron diffraction (RHEED) under an oxidative condition mixing 3–5 Pa of purified ozone delivered through a 9-mm-diameter nozzle positioned near the sample (roughly 3.5 cm distance) and 7 Pa of background oxygen. During growth the epitaxial strain is coherently maintained within the three-unit-cell (3UC) thickness (Extended Data Fig. 1d–h). The stoichiometry precision is better than 1%. Samples are cooled down at 100 °C min^{-1} under the same ozone flow, and extracted for X-ray diffraction (XRD) measurements and Pt electrode depositions with magnetron sputtering. To achieve optimal superconductivity, postannealing in the growth chamber for 30 min at 575 °C, with purified ozone of 15 Pa (flow rate roughly 10 sccm) continuously injected through the same nozzle, is critical. The samples are then cooled in the same ozone environment at 100 °C min^{-1} until reaching near room temperature. After shutting off the ozone flow, the samples are promptly transferred from the growth chamber to the load-lock chamber. Once the load-lock gate valve is closed, pure oxygen is immediately introduced to vent the load-lock chamber, ensuring a consistent oxidation environment to stabilize the superconducting samples. Extended Data Fig. 2a,b show resistivity measurement before and after postannealing, and suggest that postannealing does not cause appreciable change in lattice structures characterized by XRD.

A 3UC $La_{2.85}Pr_{0.15}Ni_2O_7$ film on $SrLaAlO_4$ substrate grown and annealed with optimal conditions shows superconductivity with onset T_C of 45 K (Fig. 1b). Films grown and annealed under suboptimal conditions (for example, different temperatures) are shown in Extended Data Fig. 2c. The resistivity–temperature (*R*–*T*) curve undergoes a two-step resistive drop, a behaviour observed previously in disordered two-dimensional (2D) superconductors that can be described as Josephson-coupled superconducting puddles[36–38]. Only temperatures below 200 K are shown, as higher temperatures under rough vacuum conditions were found to cause oxygen loss in the samples (Extended Data Fig. 3), leading to the deterioration of superconducting properties. The onset T_C is defined as the temperature at which resistivity begins to deviate from a linear fit between 50 and 60 K. The determined onset T_C = 45 K also coincides with the temperature at which resistivity shows obvious magnetic field responses, such as at 14 T (Fig. 1c). Above onset T_C, the *R*–*T* curve shows that temperature dependence deviates from a linear behaviour previously observed in pressured bulks[3] (Fig. 1d). This may indicate different disorder or doping levels in these different systems. Phonon scatterings is also an important contributor in this temperature regime. Below 20 K, resistivity reaches zero gradually, resembling a BKT behaviour (Fig. 1e), as previously seen in 2D–interfacial superconductors[39,40]. A linear fit to the $(d\ln(R)/dT)^{-2/3}$ versus *T* curve yields T_{BKT} = 9 K (Fig. 1f). The current–voltage (*I*–*V*) characteristics show power-law behaviour similar to a BKT transition[41] (Extended Data Fig. 4). By contrast, a 3UC $La_3Ni_2O_7$ film grown on the same substrate shows a

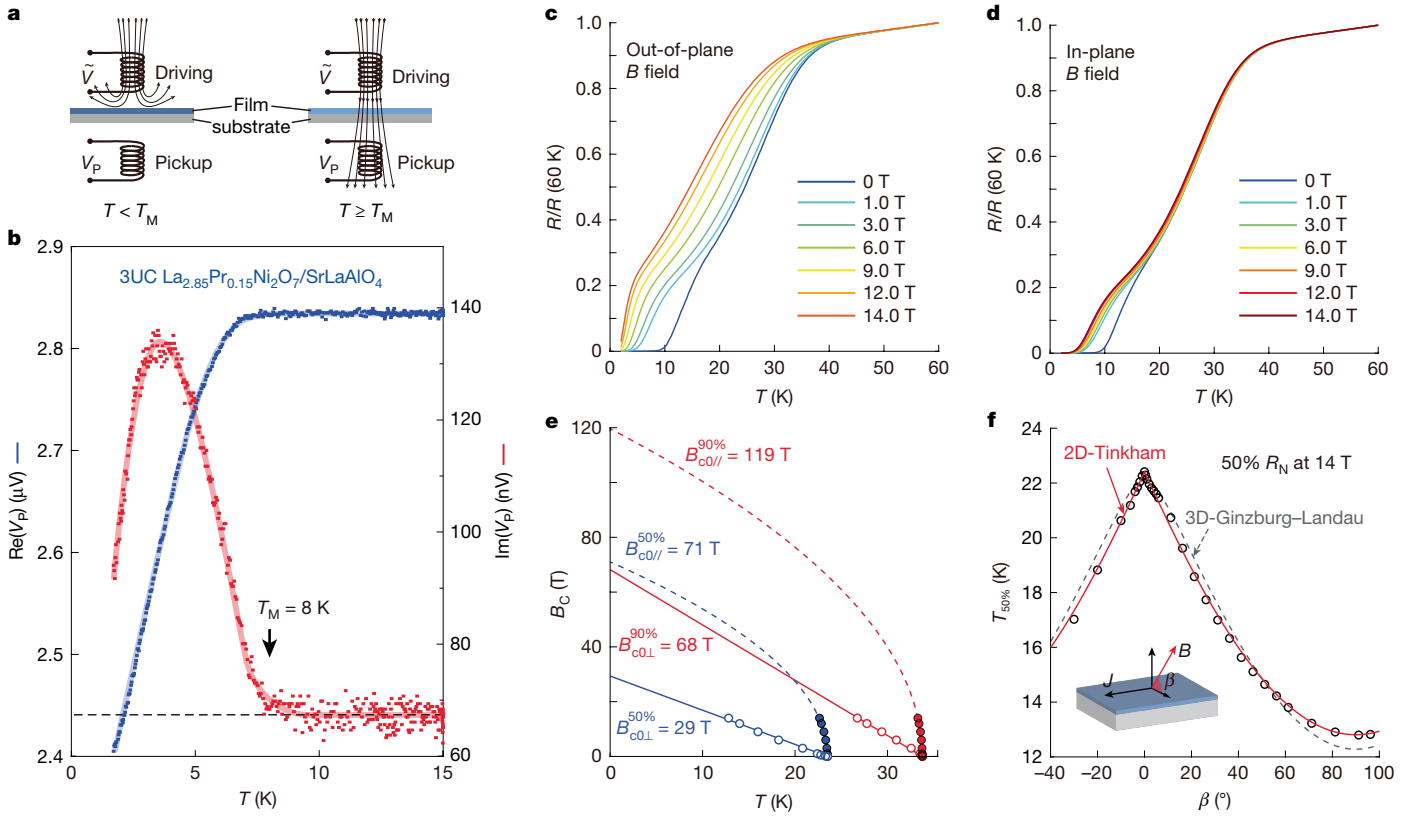

Fig. 2 | Magnetic field responses of the bilayer nickelate thin film. **a**, Schematic of a two-coil mutual inductance setup. **b**, The real (Re(V_P), blue dots) and imaginary (Im(V_P), red dots) components of the voltage in the pickup coil measured as functions of temperature on the 3UC $La_{2.85}Pr_{0.15}Ni_2O_7$ film on $SrLaAlO_4$. Shaded curves are guides to the eye. Dashed black line is a horizontal line fitting the Im(V_P) data from 10 to 15 K. T_M = 8 K is determined as the temperature at which Im(V_P) begins to deviate from the dashed black line. **c**,**d**, *R*–*T* curves with out-of-plane (**c**) and in-plane magnetic fields (**d**). **e**, In-plane (solid circles) and out-of-plane (open circles) critical fields as functions of temperature. Critical fields defined by 90% (red circles) and 50% (blue circles) of normal state resistance R_N are presented. Solid lines are linear fits. Dashed lines are fits using the Ginzburg–Landau formula. **f**, The temperature corresponding to 50% R_N at 14 T plotted as a function of the magnetic field rotation angle β. Inset shows the measurement geometry. Open circles are measured data. Red solid and grey dashed curves are the 2D-Tinkham and 3D-Ginzburg–Landau fits, respectively.

small resistive drop at roughly 10 K, without reaching zero resistance (Extended Data Fig. 5). Given the thinness of the film, interfacial disorder may play a key role in affecting superconducting phase coherence across the whole film. This may be related to that T_{BKT}, corresponding to global phase coherence, is significantly lower than the onset T_C, which is linked more closely to Cooper pairing.

Samples with and without Pr substitutions show Hall effect behaviours (Fig. 1g, raw data) markedly different from typical cuprates[42,43] (such as $La_{1.85}Sr_{0.15}CuO_4$) and infinite-layer nickelates[14–16] (such as $Nd_{0.8}Sr_{0.2}NiO_2$/$SrTiO_3$). In particular, absolute values of the Hall coefficients of both $La_3Ni_2O_7$ and $La_{2.85}Pr_{0.15}Ni_2O_7$ samples are around two orders of magnitude lower. A single band model yields roughly ten electrons or holes per Ni at 40 K, for $La_3Ni_2O_7$ or $La_{2.85}Pr_{0.15}Ni_2O_7$, respectively, which is unphysically large. In the multi-channel case, without access to ultra-high magnetic fields, the Hall effect remains linear (Extended Data Fig. 6), and the near-zero Hall coefficients indicate the coexistence of electron- and hole-like carriers. However, the role of channel-dependent mobility in the Hall effect precludes quantitative determination of electron or hole carrier concentrations, although their coexistence is evident. These results indicate the multiband nature at the Fermi level.

The Meissner diamagnetic effect is demonstrated using a mutual inductance setup[14,44,45], with the driving and pickup coils aligned vertically above and below the thin-film sample (Fig. 2a). A diamagnetic signal is observed below a Meissner temperature (T_M) of 8 K, which coincides with T_{BKT} extracted from the *R*–*T* curve within the error margin (Fig. 2b). This signifies the entrance of a true superconducting state. We extracted penetration depth λ in the order of micrometres as a function of temperature, shown in Extended Data Fig. 7. To further elucidate the dimensionality of the superconductivity, in Fig. 2c,d we show the *R*–*T* curves with varied out-of-plane and in-plane magnetic fields for the 3UC $La_{2.85}Pr_{0.15}Ni_2O_7$/$SrLaAlO_4$ sample. A strong anisotropy of magnetic response is seen. Out-of-plane and in-plane critical fields (B_c) are extracted, as defined by 90 and 50% normal state resistivity R_N, and plotted as functions of temperature (Fig. 2e). For the out-of-plane field $B_c^{\perp}$, linear fits yield a zero-temperature critical fields of 68 and 29 T, for 90 and 50% of cases, respectively. By contrast, the in-plane fields $B_c^{\parallel}$ are fitted using the 2D Ginzburg–Landau formula[46], resulting in zero-temperature critical fields of 119 and 71 T, for 90 and 50% of cases, respectively. Note that the critical field anisotropy is less pronounced than that typically observed in many 2D superconductors. However, the distinct dichotomy of linear and nonlinear temperature dependence in the out-of-plane and in-plane critical fields is hallmark of 2D superconductors[39,40], which is different from the behaviour observed in infinite-layer nickelates[46–49]. Superconducting thickness can be estimated using the formula $d_{SC} = \sqrt{(6\phi_0 B_c^{\perp}/\pi B_c^{\parallel 2})}$, where ϕ_0 is the magnetic flux quantum, yielding $d_{SC} = 4 \pm 3$ nm. Considering the 90% critical fields as the pairing breaking upper critical fields B_{c2}, coherence lengths can be estimated using the relation $\xi_0 = \sqrt{(\phi_0/2\pi B_{c2})}$, yielding in-plane coherence length $\xi_0^{\parallel} = 2.2$ nm and out-of-plane coherence length $\xi_0^{\perp} = 1.7$ nm. These coherence lengths are comparable to the out-of-plane lattice constant and the extracted d_{SC}. Setting a 14 T magnetic field, *R*–*T* curves are measured with varied rotation angle β. Temperatures at which resistivity reaches 50% of R_N ($T_{50\%}$) as a function of β are plotted in Fig. 2f. The $T_{50\%}$–β curve can be fitted well with the

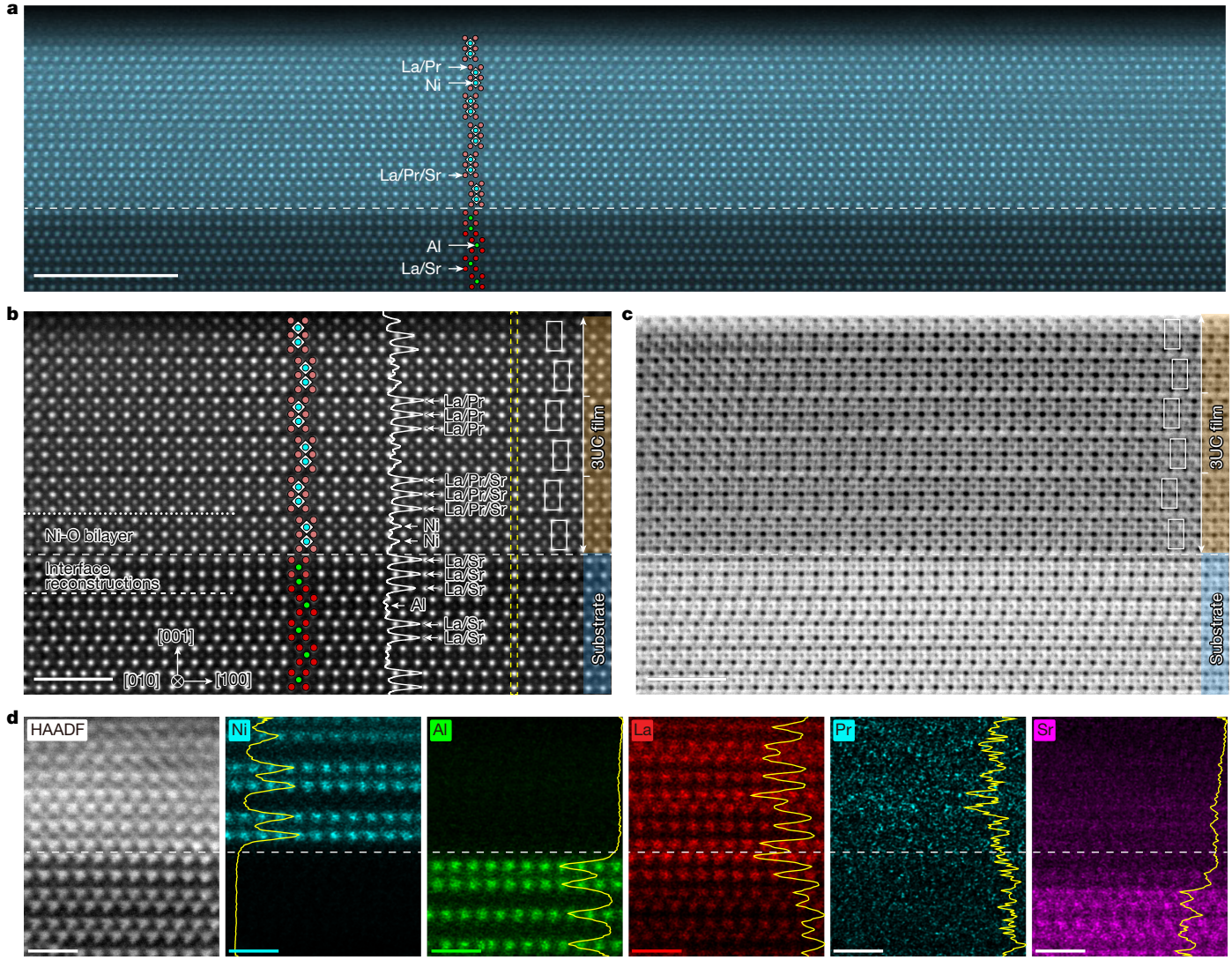

Fig. 3 | STEM of superconducting bilayer nickelate thin films. a, High-angle annular dark-field (HAADF) image of a 3UC $La_{2.85}Pr_{0.15}Ni_2O_7$/$SrLaAlO_4$ sample with a large field of view. The dashed line indicates the film-substrate interface. Note that the reduced intensity near the surface may result from damage introduced during focused ion beam sample preparation or from exposure to electron radiation during measurements. **b**,**c**, HAADF and (annular bright field) ABF images of a same field of view. The line profile of the intensity along the yellow dashed box in **b** is shown. White rectangles are guides to the eye identifying the Ni–O bilayer structures. **d**, HAADF and atomically resolved EDS (for Ni, Al, La, Pr and Sr, respectively) images of a same region of lattice in the same sample. The yellow curves are integrations of intensity in horizontal pixels. White dashed lines are guides to the eye indicating the position of the film-substrate interface. The presence of Pr in the film is spectrally distinguished from La signals, primarily by analysing the intensity at the $L\beta_1$ emission line (5,489 eV). Scale bars, 5 nm (**a**), 2 nm (**b**,**c**) and 1 nm (**d**).

Tinkham model for 2D superconductors, whereas the Ginzburg–Landau model for an anisotropic three-dimensional (3D) superconductor[50] fails to capture the cusp feature around zero angle. Because the extracted length scales are order-of-magnitude estimates, the magnetic field response data suggest that the bilayer nickelate thin-film superconductivity resides in a regime where $\xi_0 \approx d_{SC} \ll \lambda$.

Scanning transmission electron microscopy (STEM) and atomically resolved energy-dispersive X-ray spectroscopy (EDS) images reveal key structural characteristics of a superconducting 3UC $La_{2.85}Pr_{0.15}Ni_2O_7$/$SrLaAlO_4$ sample (Fig. 3). Impurity phases are not detected in the STEM image with large field of view. At the interface, the substrate undergoes reconstructions probably during the substrate treatments, forming an AlO_2 bilayer (specifically LaO-AlO_2-(La,Sr)O-AlO_2-(La,Sr)O), which acts as a template for epitaxial growth. The film growth begins with a LaO layer and follows a sequence of (La,Pr)O-NiO_2-(La,Pr)O-NiO_2-(La,Pr)O. The atomically sharp interface with no detectable interdiffusion between Ni and Al and the coherent epitaxial strain ensure that superconducting properties are preserved near the interface. Sr diffusion from the substrate into the first unit cell of the film is observed. As Sr substitution for La typically introduces hole doping, this may indicate a thinner superconducting layer (assuming hole doping is important) relative to the total film thickness, despite the single-phase structure being observed throughout the film. The smaller ionic radius of Pr^{3+} compared to La^{3+} may have facilitated the diffusion of Sr^{2+} (Extended Data Fig. 8), possibly enhancing superconductivity. Shorter Sr diffusion lengths across the interface for $La_3Ni_2O_7$/$SrLaAlO_4$ samples may lead to a reduced effective superconducting thickness, making these samples more sensitive to interfacial disorders associated with substrate surface quality, and thus more prone to insulating behaviour even in the presence of Cooper pairs (Extended Data Fig. 5). The prepeak observed in oxygen *K*-edge of electron energy loss spectroscopy indicates finite *p*–*d* hybridization in the film (Extended Data Fig. 9).

Figure 4 presents the XRD along the out-of-plane direction and reciprocal space mappings (RSMs) for $La_{2.85}Pr_{0.15}Ni_2O_7$ and $La_3Ni_2O_7$

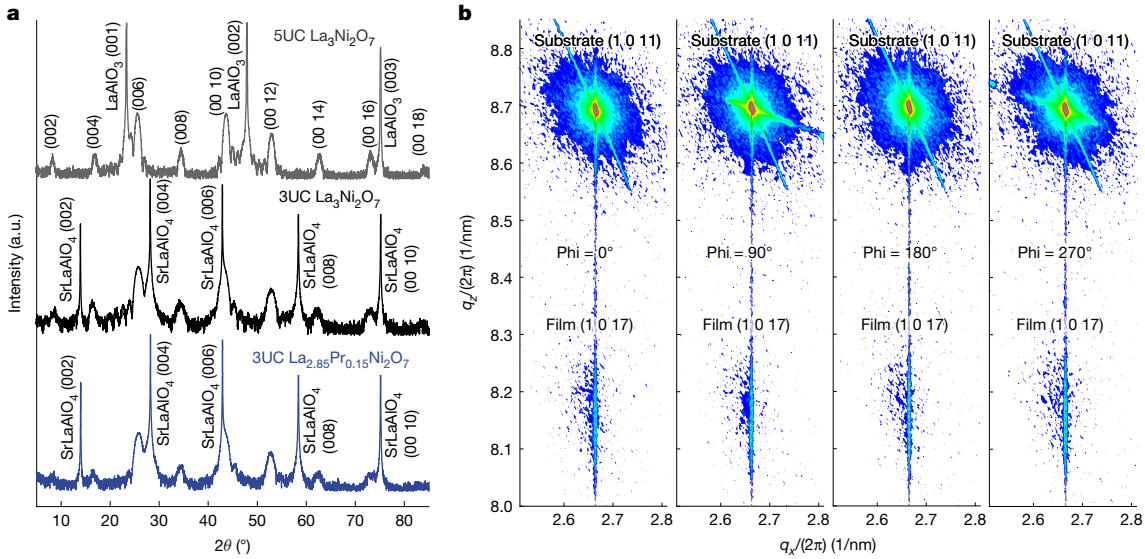

Fig. 4 | XRD and RSM of bilayer nickelate thin films. a, XRD along the out-of-plane axis for a 5UC $La_3Ni_2O_7$ film on $LaAlO_3$ substrate, a 3UC $La_3Ni_2O_7$ film on $SrLaAlO_4$ substrate and a 3UC $La_{2.85}Pr_{0.15}Ni_2O_7$ film on $SrLaAlO_4$ substrate. Note that the width difference of the peaks is related to the film thickness difference. **b**, RSMs of a 3UC $La_{2.85}Pr_{0.15}Ni_2O_7$ film on $SrLaAlO_4$ along four different phi angles. Identical q_z across the four cases reveal tetragonal phase of the film. Aligned q_x between film and substrate indicate coherent straining. a.u., arbitrary units.

films. The XRD reveals a series of well-defined diffraction peaks without indication of impurity phases, indicating high crystalline quality even with only 3–5 unit cells. The out-of-plane lattice constant of the superconducting $La_{2.85}Pr_{0.15}Ni_2O_7$ film on $SrLaAlO_4$ substrate is calculated at 20.74 Å, roughly 1% elongated compared to bulk (out-of-plane lattice constant is 20.519 Å). The non-superconducting $La_3Ni_2O_7$ film grown on $LaAlO_3$ substrate with a larger in-plane lattice constant, showing slightly smaller out-of-plane lattice constant, implying the possible role of sufficient straining for superconductivity. The presence of Kiessig fringes around the main diffraction peaks confirms that the sample has an atomically smooth surface and interface (also seen in atomic force microscope images in Extended Data Fig. 10a–d). X-ray reflectivity measurements yield film thickness of roughly 6.6 nm for 3UC $La_{2.85}Pr_{0.15}Ni_2O_7$ film on $SrLaAlO_4$ substrate, in agreement with the expectation from growth within error margins (Extended Data Fig. 10e,f). The RSMs of the superconducting 3UC $La_{2.85}Pr_{0.15}Ni_2O_7$ film along four different in-plane directions show consistent q_z values, providing evidence of a tetragonal phase. Alignment of q_x between the film and the substrate demonstrates a uniform and coherent strain state across the film. In other words, the film has the same in-plane lattice constant as the $SrLaAlO_4$ substrate (3.75 Å), corresponding to a compressive strain of roughly 2% compared to bulk (in-plane lattice constant of 3.832 Å). Owing to coherent straining, both 3UC $La_{2.85}Pr_{0.15}Ni_2O_7$ and 3UC $La_3Ni_2O_7$ films grown on $SrLaAlO_4$ substrates show nearly identical in-plane lattice constants within error bars.

In this work, we have achieved superconductivity in pure-phase RP bilayer nickelate thin films at ambient pressure with transition onset above the McMillan limit. Using the GOALL-Epitaxy method, we grew high-quality, epitaxially strained 3UC $La_{2.85}Pr_{0.15}Ni_2O_7$ films on $SrLaAlO_4$ substrates with atomically smooth surfaces and interfaces. The thin film shows an onset T_C of 45 K and a BKT-like transition behaviour with T_{BKT} = 9 K, aligning with the Meissner temperature T_M = 8 K. Magnetic responses reveal anisotropy in critical fields. Our work allows experimental investigations of the superconductivity mechanism with enhanced feasibility and lays a foundation for achieving transition temperature higher than 77 K (liquid nitrogen boiling temperature) in nickelates at ambient pressure.

During the review process, we identified parallel research efforts documenting signatures of superconductivity in $La_3Ni_2O_7$ thin films[51].

Online content

Any methods, additional references, Nature Portfolio reporting summaries, source data, extended data, supplementary information, acknowledgements, peer review information; details of author contributions and competing interests; and statements of data and code availability are available at https://doi.org/10.1038/s41586-025-08755-z.

1. Sun, H. et al. Signatures of superconductivity near 80 K in a nickelate under high pressure. *Nature* **621**, 493–498 (2023).
2. Hou, J. et al. Emergence of high-temperature superconducting phase in pressurized $La_3Ni_2O_7$ crystals. *Chin. Phys. Lett.* **40**, 117302 (2023).
3. Zhang, Y. et al. High-temperature superconductivity with zero resistance and strange-metal behaviour in $La_3Ni_2O_{7-\delta}$. *Nat. Phys.* **20**, 1269–1273 (2024).
4. Wang, G. et al. Pressure-induced superconductivity in polycrystalline $La_3Ni_2O_{7-\delta}$. *Phys. Rev. X.* **14**, 011040 (2024).
5. Wang, N. et al. Bulk high-temperature superconductivity in pressurized tetragonal $La_2PrNi_2O_7$. *Nature* **634**, 579–584 (2024).
6. Dong, Z. et al. Visualization of oxygen vacancies and self-doped ligand holes in $La_3Ni_2O_{7-\delta}$. *Nature* **630**, 847–852 (2024).
7. Yang, J. et al. Orbital-dependent electron correlation in double-layer nickelate $La_3Ni_2O_7$. *Nat. Commun.* **15**, 4373 (2024).
8. Liu, Z. et al. Electronic correlations and partial gap in the bilayer nickelate $La_3Ni_2O_7$. *Nat. Commun.* **15**, 7570 (2024).
9. Zhou, G. et al. Gigantic-oxidative atomic-layer-by-layer epitaxy for artificially designed complex oxides. *Natl Sci. Rev.* https://doi.org/10.1093/nsr/nwae429 (2024).
10. Bednorz, J. G. & Müller, K. A. Possible high T_c Superconductivity in the Ba–La–Cu–O System. *Z. Phys. B Con. Mat.* **64**, 189–193 (1986).
11. Keimer, B., Kivelson, S. A., Norman, M. R., Uchida, S. & Zaanen, J. From quantum matter to high-temperature superconductivity in copper oxides. *Nature* **518**, 179–186 (2015).
12. Lee, P. A. & Wen, X.-G. Doping a Mott insulator: physics of high-temperature superconductivity. *Rev. Mod. Phys.* **78**, 17–85 (2006).
13. Fradkin, E., Kivelson, S. A. & Tranquada, J. M. Colloquium: theory of intertwined orders in high temperature superconductors. *Rev. Mod. Phys.* **87**, 457–482 (2015).
14. Li, D. et al. Superconductivity in an infinite-layer nickelate. *Nature* **572**, 624–627 (2019).
15. Zeng, S. et al. Phase diagram and superconducting dome of infinite-layer $Nd_{1-x}SrxNiO_2$ thin films. *Phys. Rev. Lett.* **125**, 147003 (2020).
16. Li, D. et al. Superconducting dome in $Nd_{1-x}Sr_xNiO_2$ infinite layer films. *Phys. Rev. Lett.* **125**, 027001 (2020).
17. Gu, Q. et al. Single particle tunneling spectrum of superconducting $Nd_{1-x}Sr_xNiO_2$ thin films. *Nat. Commun.* **11**, 6027 (2020).
18. Wang, N. N. et al. Pressure-induced monotonic enhancement of T_c to over 30 K in superconducting $Pr_{0.82}Sr_{0.18}NiO_2$ thin films. *Nat. Commun.* **13**, 4367 (2022).
19. Ding, X. et al. Critical role of hydrogen for superconductivity in nickelates. *Nature* **615**, 50–55 (2023).
20. Lee, K. et al. Linear-in-temperature resistivity for optimally superconducting (Nd,Sr)NiO_2. *Nature* **619**, 288–292 (2023).
21. Gao, Q. et al. Magnetic excitations in strained infinite-layer nickelate $PrNiO_2$ films. *Nat. Commun.* **15**, 5576 (2024).

22. Chen, Z. et al. Electronic structure of superconducting nickelates probed by resonant photoemission spectroscopy. *Matter* **5**, 1806–1815 (2022).
23. Cheng, B. et al. Evidence for *d*-wave superconductivity of infinite-layer nickelates from low-energy electrodynamics. *Nat. Mater.* **23**, 775–781 (2024).
24. Ding, X. et al. Cuprate-like electronic structures in infinite-layer nickelates with substantial hole dopings. *Natl Sci. Rev.* **11**, nwae194 (2024).
25. Luo, Z., Hu, X., Wang, M., Wú, W. & Yao, D.-X. Bilayer two-orbital model of $La_3Ni_2O_7$ under pressure. *Phys. Rev. Lett.* **131**, 126001 (2023).
26. Liu, Y.-B., Mei, J.-W., Ye, F., Chen, W.-Q. & Yang, F. $s^{\pm}$-Wave pairing and the destructive role of apical-oxygen deficiencies in $La_3Ni_2O_7$ under pressure. *Phys. Rev. Lett.* **131**, 236002 (2023).
27. Oh, H. & Zhang, Y. H. Type-II *t–J* model and shared superexchange coupling from Hund's rule in superconducting $La_3Ni_2O_7$. *Phys. Rev. B* **108**, 174511 (2023).
28. Lu, C., Pan, Z., Yang, F. & Wu, C. Interlayer-coupling-driven high-temperature superconductivity in $La_3Ni_2O_7$ under pressure. *Phys. Rev. Lett.* **132**, 146002 (2024).
29. Yang, Q.-G., Wang, D. & Wang, Q.-H. Possible $s^{\pm}$-wave superconductivity in $La_3Ni_2O_7$. *Phys. Rev. B* **108**, L140505 (2023).
30. Wang, M., Wen, H.-H., Wu, T., Yao, D.-X. & Xiang, T. Normal and superconducting properties of $La_3Ni_2O_7$. *Chin. Phys. Lett.* **41**, 077402 (2024).
31. Zhu, Y. et al. Superconductivity in pressurized trilayer $La_4Ni_3O_{10-\delta}$ single crystals. *Nature* **631**, 531–536 (2024).
32. Puphal, P. et al. Unconventional crystal structure of the high-pressure superconductor $La_3Ni_2O_7$. *Phys. Rev. Lett.* **133**, 146002 (2024).
33. Abadi, S. N. et al. Electronic structure of the alternating monolayer-trilayer phase of $La_3Ni_2O_7$. Preprint at https://doi.org/10.48550/arXiv.2402.07143 (2024).
34. Chen, X. et al. Polymorphism in the Ruddlesden–Popper nickelate $La_3Ni_2O_7$: discovery of a hidden phase with distinctive layer stacking. *J. Am. Chem. Soc.* **146**, 3640–3645 (2024).
35. Wang, H. et al. Long-range structural order in a hidden phase of Ruddlesden-Popper bilayer nickelate $La_3Ni_2O_7$. *Inorg. Chem.* **63**, 5020–5026 (2024).
36. Yu, Y. et al. High-temperature superconductivity in monolayer $Bi_2Sr_2CaCu_2O_{8+\delta}$. *Nature* **575**, 156–163 (2019).
37. Eley, S. et al. Approaching zero-temperature metallic states in mesoscopic superconductor–normal–superconductor arrays. *Nat. Phys.* **8**, 59–62 (2012).
38. Chen, Z. et al. Carrier density and disorder tuned superconductor-metal transition in a two-dimensional electron system. *Nat. Commun.* **9**, 4008 (2018).
39. Saito, Y., Nojima, T. & Iwasa, Y. Highly crystalline 2D superconductors. *Nat. Rev. Mater.* **2**, 16094 (2017).
40. Reyren, N. et al. Superconducting interfaces between insulating oxides. *Science* **317**, 1196–1199 (2007).
41. Li, D. et al. Quasi-two-dimensional nature of high-T_c superconductivity in iron-based (Li,Fe)OHFeSe. *Chin. Phys. Lett.* **39**, 127402 (2022).
42. Hwang, H. Y. et al. Scaling of the temperature dependent Hall effect in $La_{2-x}Sr_xCuO_4$. *Phys. Rev. Lett.* **72**, 2636–2639 (1994).
43. Zhao, S. Y. F. et al. Sign reversing Hall effect in atomically thin high temperature $Bi_{2.1}Sr_{1.9}CaCu_{2.0}O_{8+\delta}$ superconductors. *Phys. Rev. Lett.* **122**, 247001 (2019).
44. Božović, I. et al. Dependence of the critical temperature in overdoped copper oxides on superfluid density. *Nature* **536**, 309–311 (2016).
45. Jiang, X. et al. Interplay between superconductivity and the strange-metal state in FeSe. *Nat. Phys.* **19**, 365–371 (2023).
46. Wang, B. Y. et al. Isotropic Pauli-limited superconductivity in the infinite-layer nickelate $Nd_{0.775}Sr_{0.225}NiO_2$. *Nat. Phys.* **17**, 473–477 (2021).
47. Ji, H. et al. Rotational symmetry breaking in superconducting nickelate $Nd_{0.8}Sr_{0.2}NiO_2$ films. *Nat. Commun.* **14**, 7155 (2023).
48. Chow, L. E. et al. Dimensionality control and rotational symmetry breaking superconductivity in square-planar layered nickelates. Preprint at https://doi.org/10.48550/arXiv.2301.07606 (2023).
49. Sun, W. et al. Evidence for anisotropic superconductivity beyond Pauli limit in infinite-layer lanthanum nickelates. *Adv. Mater.* **35**, 2303400 (2023).
50. Welp, U. et al. Angular dependence of the upper critical field of $YBa_2Cu_3O_{7-\delta}$ single crystals. *Phys. Rev. B* **40**, 5263(R) (1989).
51. Ko, E.-K. et al. Signatures of ambient pressure superconductivity in thin film $La_3Ni_2O_7$. *Nature* https://doi.org/10.1038/s41586-024-08525-3 (2024).

Methods

Growth of $La_3Ni_2O_7$ and $La_{2.85}Pr_{0.15}Ni_2O_7$ films

All samples were prepared using the gigantic-oxidative atomically layer-by-layer epitaxy (GOALL-Epitaxy) method. In the growth of $La_3Ni_2O_7$ and $La_{2.85}Pr_{0.15}Ni_2O_7$ films, which features a stacking block structure of (La,Pr)O-NiO_2-(La,Pr)O-NiO_2-(La,Pr)O, alternating laser ablation of LaO_x/$La_{0.95}Pr_{0.05}O_x$ and NiO_x targets is used to achieve atomic layer-by-layer epitaxy. Calibrating the stoichiometry relies on determining both the precise number of laser pulses and energy required to ablate a target and deposit one monolayer on substrate. In a typical growth process, the number of pulses used to ablate LaO_x/$La_{0.95}Pr_{0.05}O_x$ or NiO_x targets is between 100 and 150 pulses, providing a stoichiometric precision greater than 1%.

LaO_x, NiO_x and $La_{0.95}Pr_{0.05}O_x$ targets were prepared by sintering LaO, NiO, or stoichiometric mixtures of LaO and PrO powders at 1,100 °C for 6 h. The growth temperature and laser fluence for all samples were set to be roughly 750 °C and 1.4–1.8 J cm^{-2}. The deposition atmosphere consists of two components: purified ozone and oxygen, with partial pressures of 3 and 7 Pa, respectively. After the deposition, the samples were cooled down at 100 °C min^{-1} in the same environment to improve experimental efficiency. Cooling rates of 50 and 60 °C min^{-1} were also tested, with no significant differences in the crystalline quality observed.

Postannealing

Postannealing was performed for 30 min at 575 °C in the growth chamber for optimal superconductivity, with purified ozone of roughly 15 Pa (flow rate roughly 10 sccm) delivered through a 9-mm-diameter nozzle. The samples were cooled in the same ozone environment at 100 °C min^{-1}. The samples were extracted from the chamber until they reached near room temperature. Annealing has minimal effect on crystalline quality. Sample temperatures in the growth chamber were measured by pyrometer from the back of the inconel600 sample holder.

Substrate preparation

For clean surface preparation of the $SrLaAlO_4$ (001) substrates (MTI), annealing was performed by putting a $LaAlO_3$ substrate on a $SrLaAlO_4$ substrate face to face in the atmospheric or 1 atm oxygen conditions at 1,030 or 1,080 °C for 2 h. Treated substrates may show either double or single termination surfaces, which do not significantly affect the film growth, strain or lattice structure. Oxygen stoichiometry in the films is predominantly controlled during postannealing.

Low-temperature transport measurements

Electric transport measurements were performed in a closed-cycle helium-free system (base temperature roughly 1.8 K). Hall bar electrodes with Pt were evaporated by magnetron sputtering with a pre-patterned hard shadow mask covered on 5- × 5-mm samples. The four terminal electrical measurements were carried out through the standard lock-in technique with an a.c. current of 0.5 μA (13 Hz) for resistance measurements and 10 μA for Hall measurements. The transition temperatures under different magnetic fields are extracted from the resistivity versus magnetic field curves shown in Fig. 2c,d. The normal state resistivity R_N at a certain temperature is determined by linear extrapolation from the 50–60-K range. Samples experience oxygen loss in vacuum above 200 K and in atmosphere at ambient temperature, which can be characterized by resistance increase. Meanwhile, lattice structures characterized by XRD do not show noticeable differences (Extended Data Fig. 3).

Mutual inductance measurements

The superconducting thin-film samples were placed tightly between the collinear driving and pickup coils, similar to refs. 14,44,45. The driving coil and pickup coil are both made using 30-μm-diameter wires and have identical specifications. Each coil has an outer diameter of 1.5 mm, an inner diameter of 0.5 mm and a height of roughly 2.5 mm and 800 turns, resulting in a self-inductance of 1 mH. The driving coil was driven with a 20-kHz 5-μA alternating current. The voltage across the pickup coil is measured by a lock-in amplifier.

STEM

STEM HAADF and ABF imaging of the superconducting $La_{2.85}Pr_{0.15}Ni_2O_7$ film were photographed using a FEI Titan Themis G2 at 200 kV. A double spherical-aberration corrector and a high-brightness field-emission gun (X-FEG) with a monochromator is installed onto this microscope to enhance image resolution and contrast. The inner and outer collection angles for the STEM images (β1 and β2) were 90 and 200 mrad for HAADF images, and 12 and 23 mrad for ABF images, respectively. The semiconvergence angle was maintained at 25 mrad, and the beam current was adjusted to about 40 pA for HAADF/ABF imaging and the EDS chemical analyses. EDS data were obtained using the Super X System in STEM mode. Electron energy loss spectra were acquired using a FEI Themis Z equipped with a high stability stage and a Gatan Quantum ER/965 spectrometer. The microscope was operated at 200 kV with a beam current of 200 pA. The probe currents are controlled less than 200 pA to minimize radiation damage with the scan parameters used: roughly 1-Å probe, roughly 9-$Å^2$ scan pixel size (applied 16 × 16 subpixel scan) and 300 μs per pixel dwell time. The cross-section STEM specimens were prepared using a FEI Helios 600i dual-beam focused ion beam and scanning electron microscope machine. Before extraction and thinning, electron beam-deposited platinum and ion beam-deposited carbon were used to protect the sample surface from ion beam damage. All operations were done at room temperature.

XRD

Crystallographic characterization of thin-film specimens was performed using an automated multipurpose X-ray diffractometer (SmartLab, Rigaku Corporation), encompassing θ–2θ scans and RSMs. After the in-plane sample alignment, the RSMs around (1 0 11), (0 1 11), (−1 0 11) and (0 −1 11) $SrLaAlO_4$ Bragg reflections were measured by rotating the phi axis using the Hypix-3000 2D detector.

Synchrotron soft XAS

The valence characterization of thin film was conducted at the BL07U beamline at the Shanghai Synchrotron Radiation Facility. All X-ray absorption spectroscopy (XAS) spectra at the Ni L_2-edge were taken in the total electron yield configuration with an X-ray normal incident on the sample surface. These XAS were normalized such that the intensity at the pre-edge and the postedge were 0 and 1, respectively. Owing to the overlap between the tail of the La M_4-line and the Ni L_3-edge, the valence difference of Ni between a superconducting $La_{2.85}Pr_{0.15}Ni_2O_7$/$SrLaAlO_4$ sample and a superconducting $Nd_{0.8}Sr_{0.2}NiO_2$/LSAT sample is demonstrated by comparing the spectra of Ni L_2-edge.

Data availability

Source data are provided with this paper.

Acknowledgements We acknowledge the discussions with G.-M. Zhang, D.-X. Yao and H. Yuan. This work was supported by the National Key R&D Program of China (grant no. 2022YFA1403101), the Natural Science Foundation of China (grants 92265112, 12374455 and 52388201), the Guangdong Provincial Quantum Science Strategic Initiative (grants GDZX2401004 and GDZX2201001), the Shenzhen Municipal Funding Co-Construction Program Project (grants SZZX2401001 and SZZX2301004) and the Shenzhen Science and Technology Program (grant KQTD20240729102026004). H.W. acknowledges support by the China Postdoctoral Science Foundation (grants GZB20240294 and 2024M751287). W.-Q.C. acknowledges the support by Center for Computational Science and Engineering at Southern University of Science and Technology.

Author contributions Q.-K.X. and Z.C. supervised the project. Z.C. initiated the study and coordinated the research efforts. G.Z., W.L. and Z.N. performed thin-film growth with assistance from Y.C. H.W. performed low-temperature measurements and analysis. Y.L. and

H.H. contributed on STEM analysis. H.H. contributed on XRD analysis. W.-Q.C. provided theoretical support. Y.-J.S. provided support in data interpretation. Z.C. wrote the manuscript with key input from Q.-K.X. and all other authors. G.Z., W.L., H.W. and Z.N. contributed equally to this work.

Competing interests The authors declare no competing interests.

Additional information

Correspondence and requests for materials should be addressed to Qi-Kun Xue or Zhuoyu Chen.

Peer review information *Nature* thanks Zhen Chen, Liang Qiao and Huiqiu Yuan for their contribution to the peer review of this work.

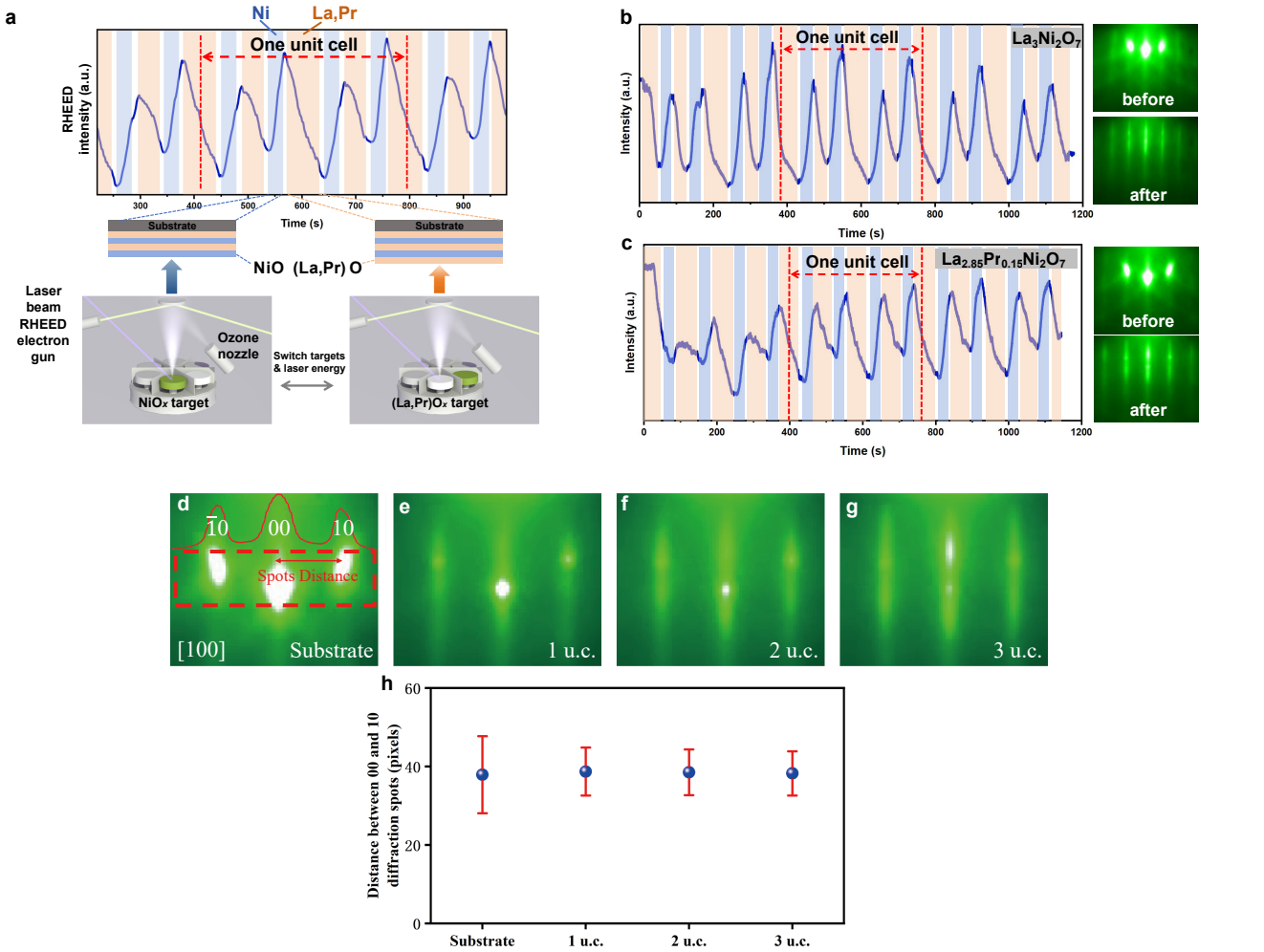

Extended Data Fig. 1 | Growth. a, Schematic of synthesizing $(La,Pr)_3Ni_2O_7$ on $SrLaAlO_4$ with gigantic-oxidative atomically layer-by-layer epitaxy (GOALL-Epitaxy). **b** and **c**, RHEED oscillations and patterns of $La_3Ni_2O_7$ and $La_{2.85}Pr_{0.15}Ni_2O_7$ growth on $SrLaAlO_4$. Blue and orange blocks represent the growth of $LaO_x/(La_{0.95}Pr_{0.05})O_x$ and NiO_x layer, respectively. **d**-**g**, Time evolution of RHEED pattern during the growth of $La_{2.85}Pr_{0.15}Ni_2O_7$ film on $SrLaAlO_4$ substrate. RHEED pattern of the substrate $SrLaAlO_4$ (d), 1 unit cell of $La_{2.85}Pr_{0.15}Ni_2O_7$ (e), 2 unit cells (f) and 3 unit cells (g), respectively along [100] direction. Red solid line in (d) represents the intensity profile, which is obtained by integrating the intensity vertically in the rectangular area marked with red dashed line. **h**, Evolution of the distance between 00 and 01 diffraction spots, which is determined by the peak position of the intensity profile and the error bar is calculated by the FWHM of the peak.

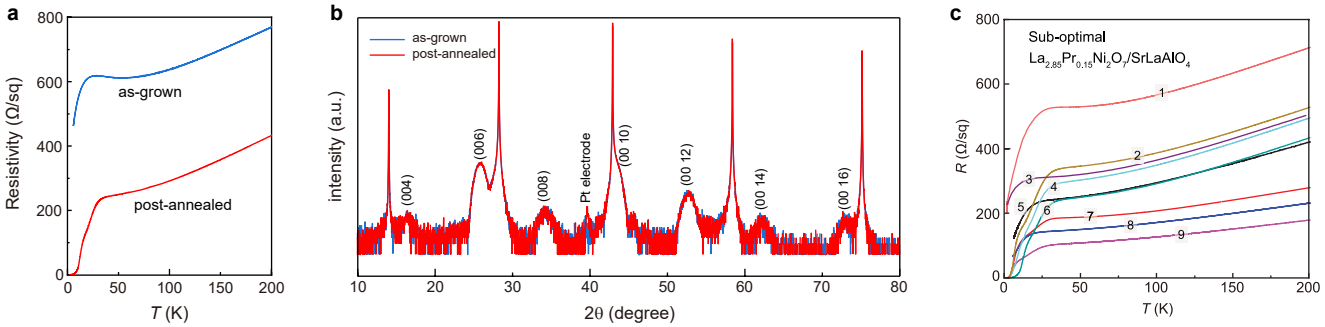

Extended Data Fig. 2 | Post-annealing. a, Resistivity-versus-temperature curves of a 3UC $La_{2.85}Pr_{0.15}Ni_2O_7/SrLaAlO_4$ sample before and after pure ozone flow annealing. This is a different sample from the one shown in Figs. 1 and 2 in the main text. **b**, X-ray diffraction (XRD) of the same sample shown in (**a**) before and after pure ozone flow annealing. **c**, Resistivity-temperature curves for $La_{2.85}Pr_{0.15}Ni_2O_7$ films on $SrLaAlO_4$ substrates with different annealing conditions as follows. Sample 1 (3UC): 400 °C for 30 mins, with an O_3 pressure of 1.57×10^{-1} mbar. Sample 2 (3UC): 500 °C for 30 mins, with an O_3 pressure of 1.52×10^{-1} mbar. Sample 3 (3UC): 700 °C for 30 mins, with an O_3 pressure of 1.10×10^{-1} mbar. Sample 4 (3UC): 600 °C for 30 mins, with an O_3 pressure of 1.00×10^{-1} mbar. Sample 5 (3UC): 600 °C for 30 mins, with an O_3 pressure of 1.38×10^{-1} mbar. Sample 6 (3UC): 600 °C for 30 mins, with an O_3 pressure of 1.38×10^{-1} mbar. Sample 7 (3UC): 600 °C for 30 mins, with an O_3 pressure of 1.30×10^{-1} mbar. Sample 8 (6UC): 700 °C for 30 mins, with an O_3 pressure of 1.67×10^{-1} mbar. Sample 9 (6UC): 700 °C for 30 mins, with an O_3 pressure of 2.03×10^{-1} mbar. The growth conditions for all films were identical as described in the methods section.

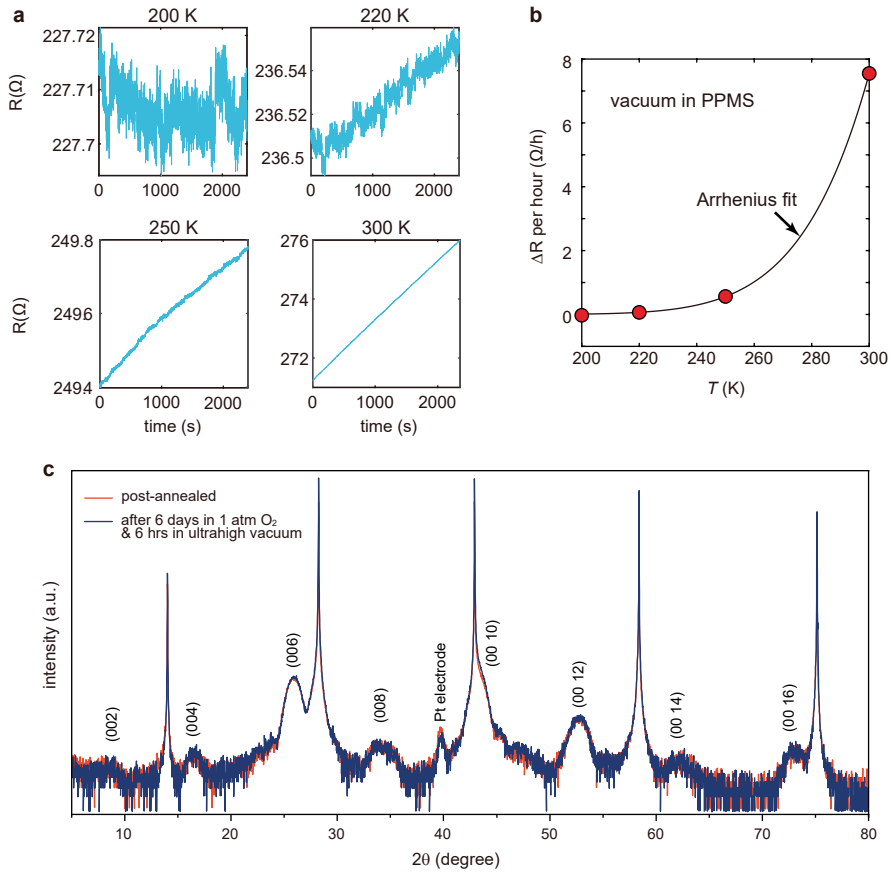

Extended Data Fig. 3 | Oxygen loss. a, Resistance changes as functions of time, with sample maintained at vacuum and different temperature inside the quantum design physical property measurement system (PPMS). **b**, An Arrhenius fit yields an activation energy of 0.34 eV for the oxygen loss process. **c**, XRD of the same sample shown in Figs. 1 and 2 in the main text after post-annealing and after 6 h in ultrahigh vacuum and 6 days in 1 atm O_2 and at ambient temperature. Resistance increase rate in 1 atm O_2 at ambient temperature is approximately 2 Ω per hour.

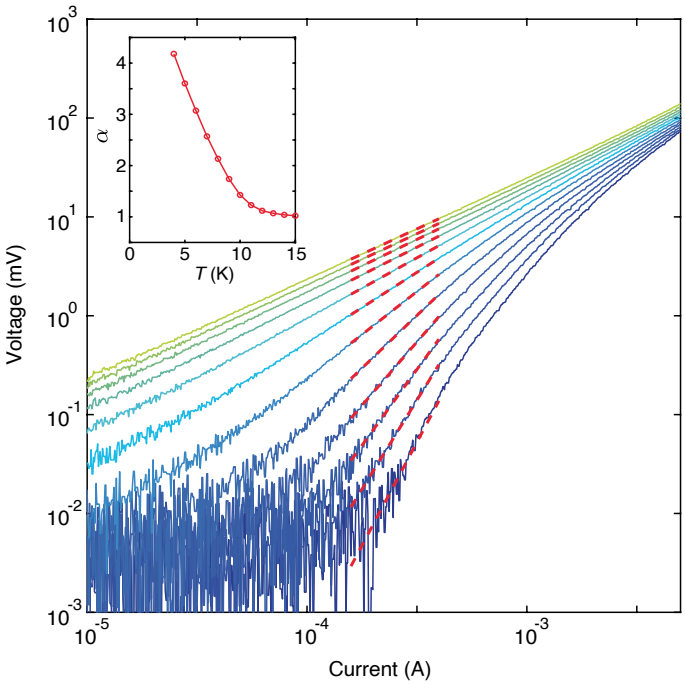

Extended Data Fig. 4 | Current-voltage (*I-V*) characteristics. *I-V* curves from 4 K to 15 K, with 1 K interval. Dashed red lines are linear fits to the log-log *I-V* curves. Inset: the power law exponent α obtained from the fit as a function of temperature. It is important to note that, due to the significant heating effect caused by the applied current (a result of the high critical current associated with the elevated T_c), the actual sample temperatures are higher than the recorded values.

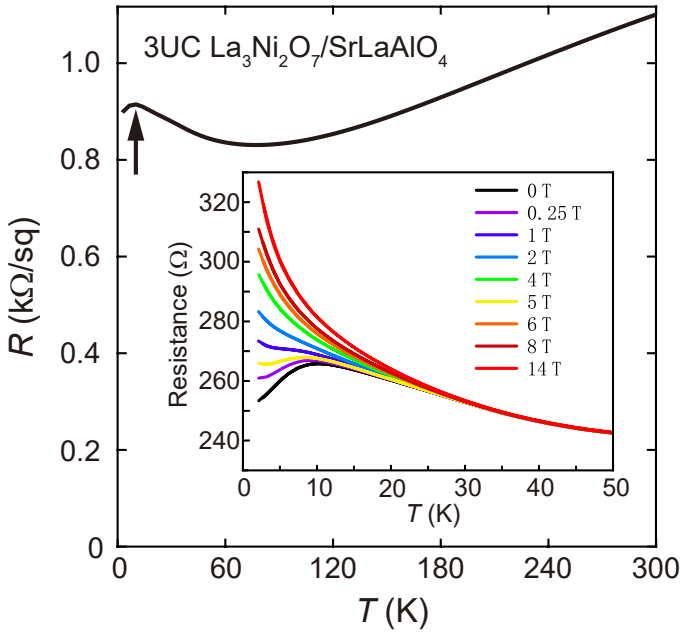

Extended Data Fig. 5 | Sample without Pr. Resistivity-temperature curve and magnetic field responses (inset) for a 3UC $La_3Ni_2O_7$ film on $SrLaAlO_4$.

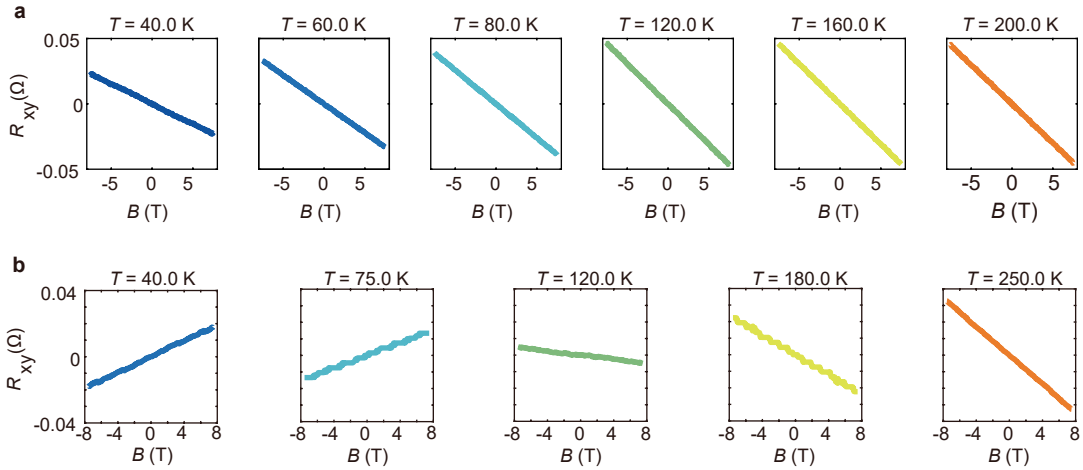

Extended Data Fig. 6 | Hall effect raw data. a, 3UC $La_{2.85}Pr_{0.15}Ni_2O_7$ film on $SrLaAlO_4$. **b**, 3UC $La_3Ni_2O_7$ film on $SrLaAlO_4$.

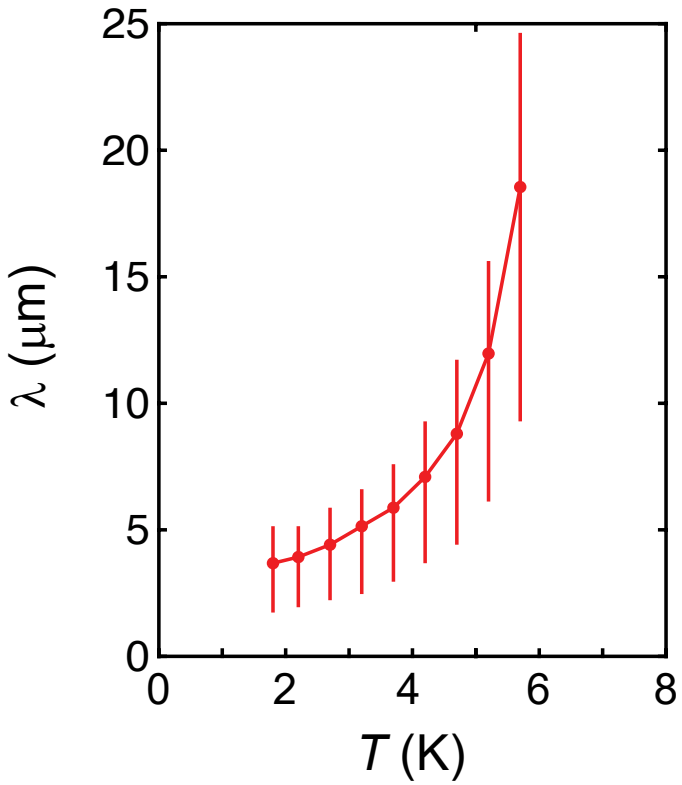

Extended Data Fig. 7 | Penetration depth. Extracted penetration depth λ as a function of temperature from mutual inductance measurements assuming superconducting thickness of 4 ± 3 nm. The flux-leak is lower than 2% in our measurement setup as calibrated by a 5 mm × 5 mm × 0.5 mm Nb plate under 2 K.

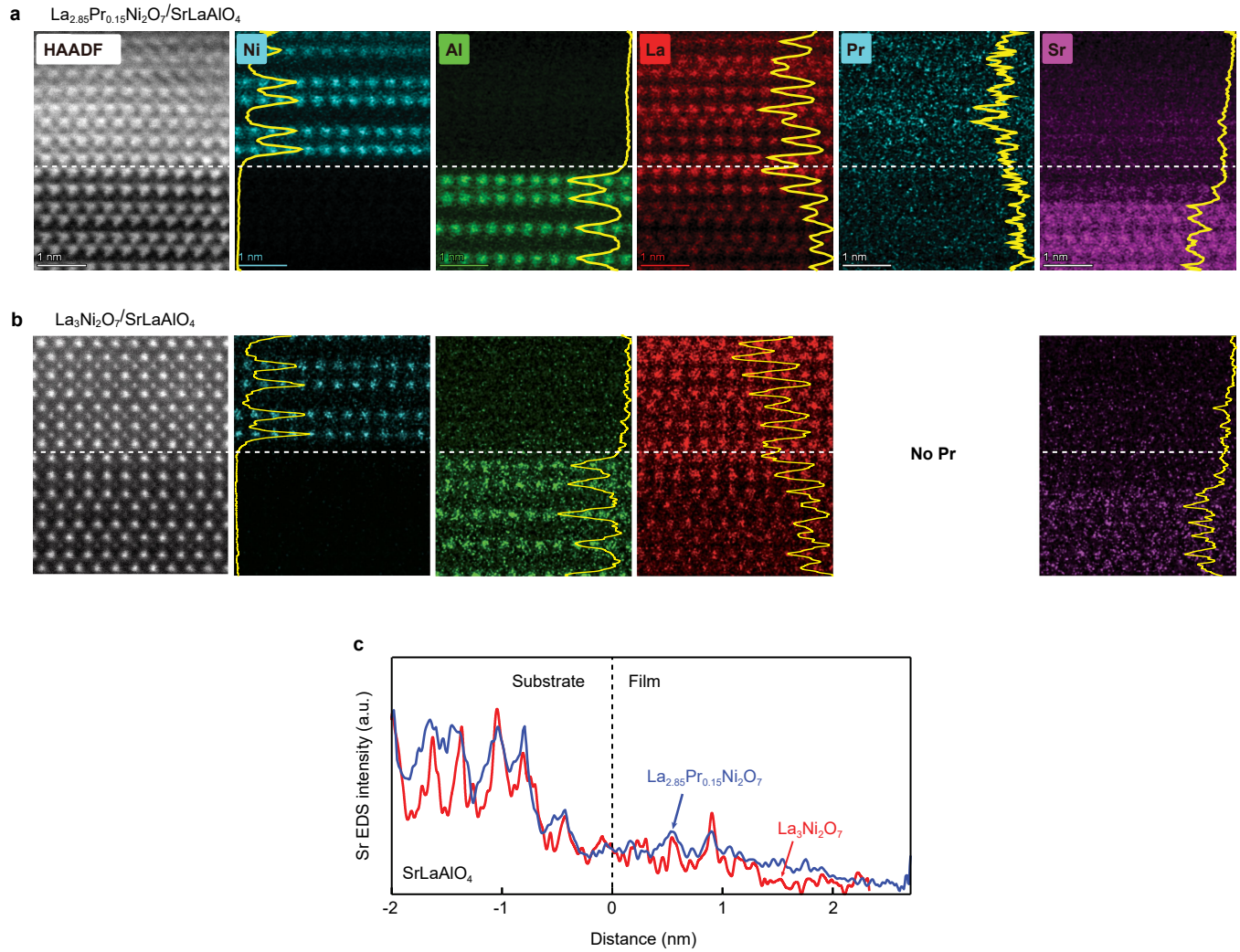

Extended Data Fig. 8 | Sr interfacial diffusion. STEM HAADF and atomically-resolved EDS of an 3UC $La_{2.85}Pr_{0.15}Ni_2O_7/SrLaAlO_4$ superconducting sample (**a**) and a 3UC $La_3Ni_2O_7/SrLaAlO_4$ sample (**b**). Data in **a** are the same set of data as shown in Fig. 3d in the main text. **c**, Sr EDS intensity for both samples as a function of distance across the interface.

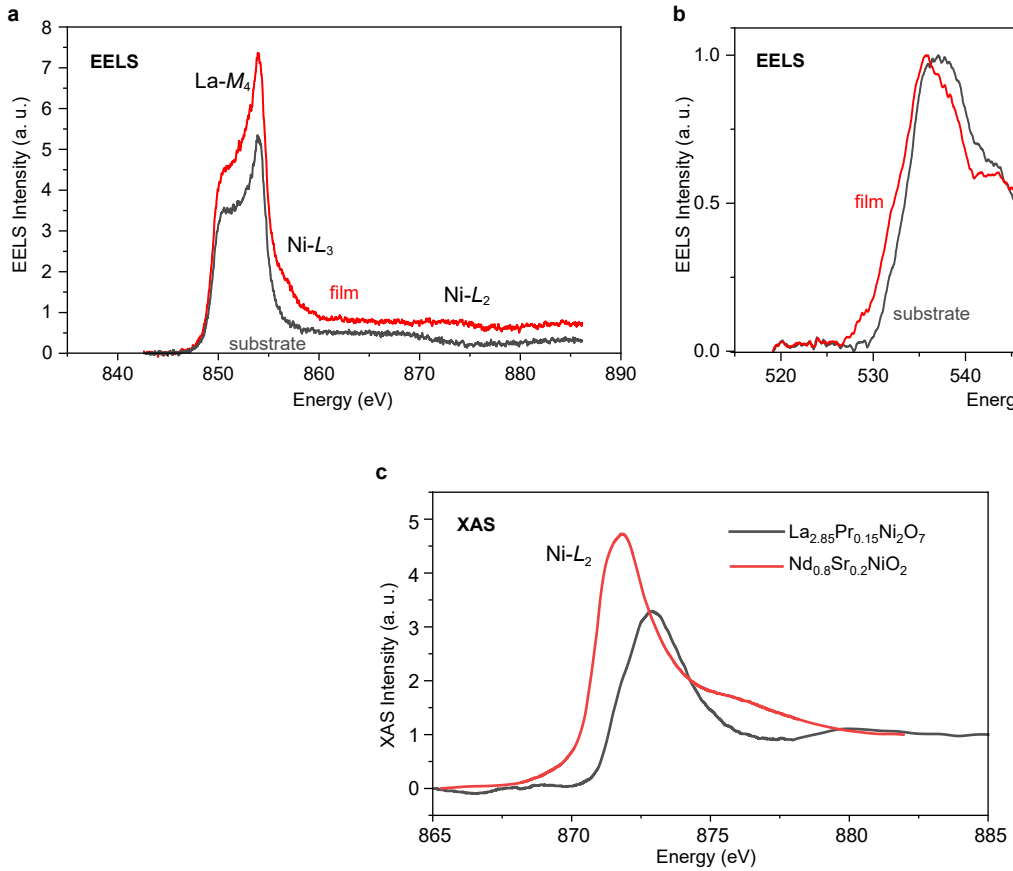

Extended Data Fig. 9 | Absorption spectroscopy. Electron energy loss spectroscopy (EELS) of Ni L (**a**) and O *K* (**b**) edges, comparing film and substrate, in an annealed 3UC $La_{2.85}Pr_{0.15}Ni_2O_7/SrLaAlO_4$ superconducting sample. **c**, Synchrotron X-ray absorption spectroscopy (XAS) spectra of Ni-L_2 edge comparing a superconducting $La_{2.85}Pr_{0.15}Ni_2O_7/SrLaAlO_4$ sample (same sample shown in Fig. 1) and a superconducting $Nd_{0.8}Sr_{0.2}NiO_2/(LaAlO_3)_{0.3}(Sr_2TaAlO_6)_{0.7}$ sample.

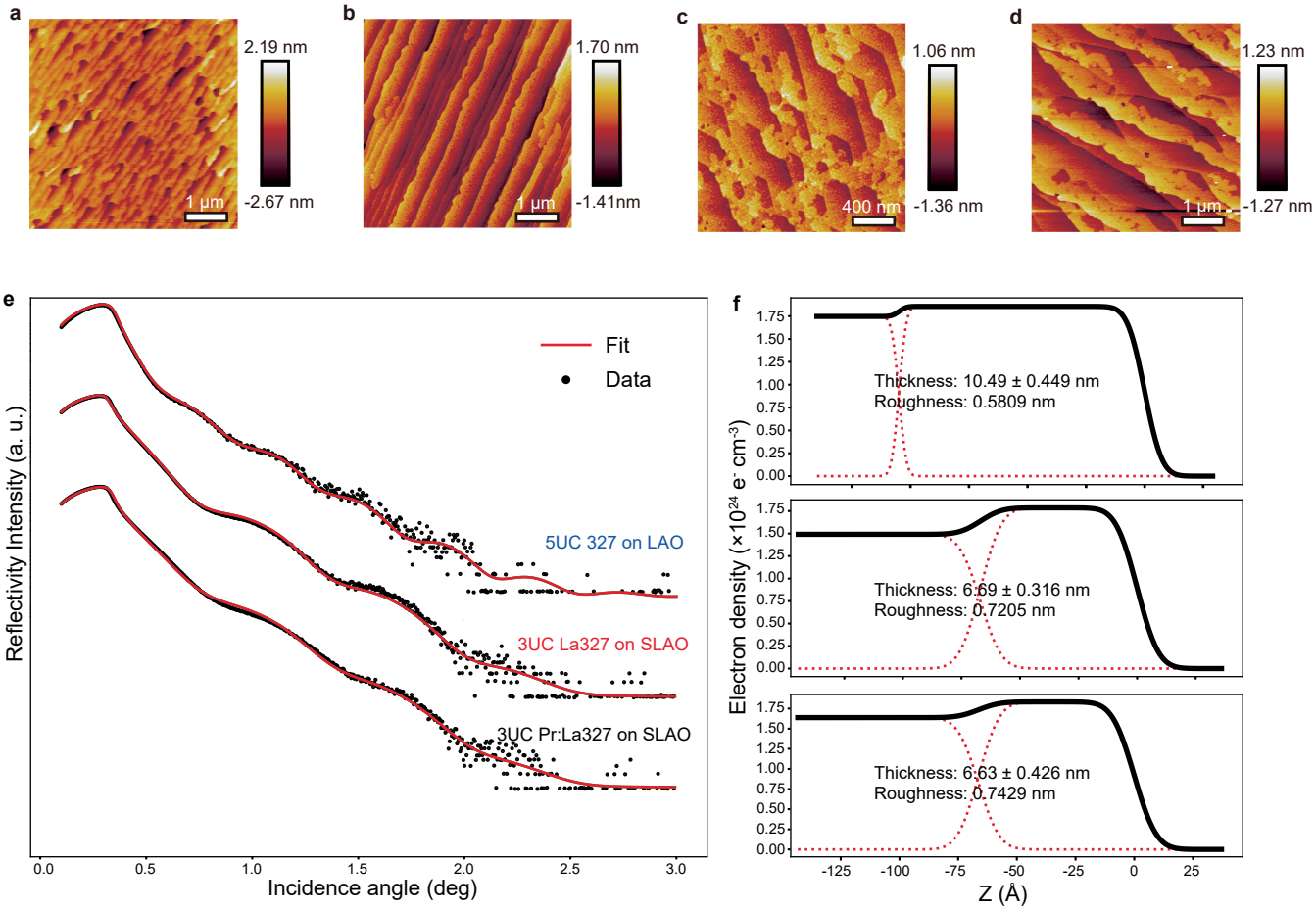

Extended Data Fig. 10 | Surface and thickness. a,**b**, Atomic force microscope (AFM) image of the $SrLaAlO_4$ substrate annealed at 1030 °C and 1080 °C, respectively. The root-mean-square roughness is 536.6 pm and 439.6 pm, respectively. **c**, AFM image of a 3UC $La_3Ni_2O_7$ film on $SrLaAlO_4$ substrate. The root-mean-square roughness is 308.6 pm. **d**, AFM image of a 3UC $La_{2.85}Pr_{0.15}Ni_2O_7$ film on $SrLaAlO_4$ substrate. The root-mean-square roughness is 407.3 pm. **e**, X-ray reflectivity (XRR) of 5UC $La_3Ni_2O_7/LaAlO_3$ (top), 3UC $La_3Ni_2O_7/SrLaAlO_4$ (middle) and 3UC $La_{2.85}Pr_{0.15}Ni_2O_7/SrLaAlO_4$ (bottom) films. **f**, The relationship between electron density and thickness obtained by fitting the XRR results. The film thickness and surface roughness obtained by fitting are also listed.

Terms and Conditions

Springer Nature journal content, brought to you courtesy of Springer Nature Customer Service Center GmbH (“Springer Nature”).
Springer Nature supports a reasonable amount of sharing of research papers by authors, subscribers and authorised users (“Users”), for small-scale personal, non-commercial use provided that all copyright, trade and service marks and other proprietary notices are maintained. By accessing, sharing, receiving or otherwise using the Springer Nature journal content you agree to these terms of use (“Terms”). For these purposes, Springer Nature considers academic use (by researchers and students) to be non-commercial.
These Terms are supplementary and will apply in addition to any applicable website terms and conditions, a relevant site licence or a personal subscription. These Terms will prevail over any conflict or ambiguity with regards to the relevant terms, a site licence or a personal subscription (to the extent of the conflict or ambiguity only). For Creative Commons-licensed articles, the terms of the Creative Commons license used will apply.
We collect and use personal data to provide access to the Springer Nature journal content. We may also use these personal data internally within ResearchGate and Springer Nature and as agreed share it, in an anonymised way, for purposes of tracking, analysis and reporting. We will not otherwise disclose your personal data outside the ResearchGate or the Springer Nature group of companies unless we have your permission as detailed in the Privacy Policy.
While Users may use the Springer Nature journal content for small scale, personal non-commercial use, it is important to note that Users may not:

1. use such content for the purpose of providing other users with access on a regular or large scale basis or as a means to circumvent access control;
2. use such content where to do so would be considered a criminal or statutory offence in any jurisdiction, or gives rise to civil liability, or is otherwise unlawful;
3. falsely or misleadingly imply or suggest endorsement, approval , sponsorship, or association unless explicitly agreed to by Springer Nature in writing;
4. use bots or other automated methods to access the content or redirect messages
5. override any security feature or exclusionary protocol; or
6. share the content in order to create substitute for Springer Nature products or services or a systematic database of Springer Nature journal content.

In line with the restriction against commercial use, Springer Nature does not permit the creation of a product or service that creates revenue, royalties, rent or income from our content or its inclusion as part of a paid for service or for other commercial gain. Springer Nature journal content cannot be used for inter-library loans and librarians may not upload Springer Nature journal content on a large scale into their, or any other, institutional repository.
These terms of use are reviewed regularly and may be amended at any time. Springer Nature is not obligated to publish any information or content on this website and may remove it or features or functionality at our sole discretion, at any time with or without notice. Springer Nature may revoke this licence to you at any time and remove access to any copies of the Springer Nature journal content which have been saved.
To the fullest extent permitted by law, Springer Nature makes no warranties, representations or guarantees to Users, either express or implied with respect to the Springer nature journal content and all parties disclaim and waive any implied warranties or warranties imposed by law, including merchantability or fitness for any particular purpose.
Please note that these rights do not automatically extend to content, data or other material published by Springer Nature that may be licensed from third parties.
If you would like to use or distribute our Springer Nature journal content to a wider audience or on a regular basis or in any other manner not expressly permitted by these Terms, please contact Springer Nature at

onlineservice@springernature.com